Heat Mass Transfer
DOI 10.1007/s00231-017-2031-6

ORIGINAL

Numerical simulation of superheated vapor bubble rising in stagnant liquid

N. Samkhaniani[1] · M. R. Ansari[1]

Received: 30 May 2016 / Accepted: 27 March 2017

Abstract In present study, the rising of superheated vapor bubble in saturated liquid is simulated using volume of fluid method in OpenFOAM cfd package. The surface tension between vapor–liquid phases is considered using continuous surface force method. In order to reduce spurious current near interface, Lafaurie smoothing filter is applied to improve curvature calculation. Phase change is considered using Tanasawa mass transfer model. The variation of saturation temperature in vapor bubble with local pressure is considered with simplified Clausius–Clapeyron relation. The couple velocity–pressure equation is solved using PISO algorithm. The numerical model is validated with: (1) isothermal bubble rising and (2) one-dimensional horizontal film condensation. Then, the shape and life time history of single superheated vapor bubble are investigated. The present numerical study shows vapor bubble in saturated liquid undergoes boiling and condensation. It indicates bubble life time is nearly linear proportional with bubble size and superheat temperature.

List of symbols

A_b	Bubble area (m^2)
Bo	Bond number ($\frac{g(\rho_L-\rho_g)D_0^2}{\sigma}$) (–)
C_α	Compression factor (–)
C	Specific heat (J/kg K)
C_d	Drag coefficient (–)
D_{eq}	Equivalent diameter (M)
D_0	Bubble initial diameter (M)
E	Numerical error
$\overrightarrow{g}$	Gravity acceleration (m/s^2)
H_{LG}	Latent heat (J/kg)
k	Thermal conductivity (W/m K)
M	Molar mass (kg/K mol)
$\dot{m}'''$	Condensate mass flow rate per unit volume (kg/m^3 s)
Mo	Morton number ($\frac{g(\rho_L-\rho_g)\mu_L^4}{\rho_L^2\sigma^3}$) (–)
P	Pressure (Pa)
R	Specific gas constant ($\frac{R_{universal}}{M}$) (J/kg K)
Re	Reynolds number ($\frac{\rho_L U_t D_0}{\mu_L}$) (–)
T	Temperature (K)
$\overrightarrow{U}$	Velocity (m/s)
$\overrightarrow{U_b}$	Bubble velocity (m/s)
$\overrightarrow{U_c}$	Compressive velocity (m/s)
$\overrightarrow{U_{rel}}$	Relative velocity (m/s)
U_t	Terminal velocity (m/s)
V_b	Bubble volume (m^3)

Greek symbols

α	Volume fraction factor (–)
δ_f	Film thickness (m)
κ	Interface curvature (m^{-1})
μ	Dynamic viscosity (Pa s)
ν	Kinematic viscosity (m^2/s)
ρ	Density (kg/m^3)

Subscripts

G	Gas (vapor) phase
L	Liquid phase
Sat	Saturation condition
Sup	Superheated condition

✉ M. R. Ansari
mra_1330@modares.ac.ir

N. Samkhaniani
nima.samkhaniani@gmail.com; nima.samkhaniani@modares.ac.ir

[1] Faculty of Mechanical Engineering, Tarbiat Modares University, P.O. Box 14117 13116, Tehran, Islamic Republic of Iran

Published online: 03 April 2017

1 Introduction

Bubble flows are frequently applied in many industrial processes which can aid heat and mass transfer. The bubble rising is one of the fundamental issues in the two phase flow. It is encountered in many industrial applications such as bubble columns or nuclear reactors. In nuclear reactors, the bubble dynamics can greatly influence the reactivity feedback characteristics of coolant which brings more challenges for reactor safety analysis. The overall heat and mass transfer is affected by the size of bubble, pressure inside the gaseous phase, bubble–bubble interaction, rise velocity and trajectory. In the process of vapor bubble rising in saturated liquid, the vapor bubble size, shape and void fraction change continuously. The mechanism governs on vapor bubble rising is far different from air bubble rising. In order to understand the boiling flow, it is a challenge to obtain an extensive knowledge on the vapor bubbles behavior.

Different aspects of bubble rising such as terminal velocity, bubble shape and bubble trajectory have extensively investigated over past decades [16, 25]. One of the prior study in this field is grace chart [16] which is classified the different shapes of bubbles rising in a stagnant liquid based on the following dimensionless numbers:

$$Re = \frac{\rho_L U_t D_0}{\mu_L} \tag{1}$$

$$Bo = \frac{g(\rho_L - \rho_g)D_0^2}{\sigma} \tag{2}$$

$$Mo = \frac{g(\rho_L - \rho_g)\mu_L^4}{\rho_L^2 \sigma^3} \tag{3}$$

Two extra dimensionless numbers of viscosity ratio (ν_L/ν_G) and density ratio (ρ_L/ρ_G) are obtained from dimensional analysis. Bhaga [11] presented a bubble shape chart with extra bubble regimes. Bhaga chart is displayed in Fig. 1 and described in Table 1. Since the work of Bhaga, a number of further experimental studies on bubble rising on unconfined domain have been conducted [17, 27, 29, 42].

In recent years, advances in computational capacity and improvement in numerical simulations increases the simulations of single bubble rising. The shape of bubbles was simulated using different interface tracking methods such as front tracking (FT) [36], level set (LS) [6], volume of fluid (VOF) [18, 39] and lattice-boltzmann [5]. Additionally, hybrid methods such as CLSVOF [14] or VOSET [7] were employed. The numerical results were compared with Bhaga [11] and Grace charts [16]. The

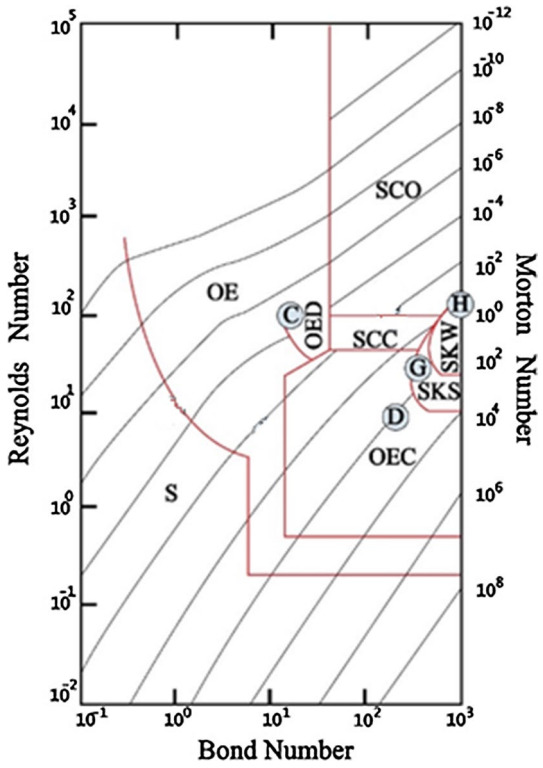

Fig. 1 Bhaga bubble regime map [11], {C, H, G, D} are selected conditions for simulation in Sect. 2.3.1

Table 1 Bubble regimes in Bhaga map [11]

Abbreviation	Table description
S	Spherical
OE	Oblate ellipsoid
OED	Oblate ellipsoid disk-like
OEC	Oblate ellipsoid cap
SCC	Spherical cap with closed steady wake
SCO	Spherical cap with open unsteady wake
SKS	Skirted with smooth, steady skirt
SKW	Skirted with wavy, unsteady skirt

effect of different parameters such as density ratio, viscosity ratio, Bond number and Reynolds number on bubble dynamics, bubble break and merge was studied [21, 22, 33, 46, 48].

When vapor bubble rises up in stagnant liquid in pool boiling, phase change happens, therefore, the heat transfer is accompanied with mass transfer in vapor bubble rising. This process is far different from usual studies of mass transfer across the interface in isothermal bubble rising which investigates containment or inert gas [4, 12, 31] or studies on heat transfer in bubble rising [12] which

is usually limited to understandings the role of temperature gradient on surface tension (Marangoni effect) in low gravity conditions [2, 3].

Pool boiling is usually classified into two major regimes of subcooled boiling and saturated boiling. There are several experimental and numerical analyses on bubble behavior in subcooled boiling. Sideman and Hirasch [43] studied free rising of the isopentane condensing bubbles at subcooled water. Chen and Mayinger [15] studied the heat transfer at the interface of condensing vapor bubble in a subcooled liquid of the same substances with ethanol, propane, R113 and water. Harada [19] carried out the visualization experiments to investigate the dynamics of vapor bubbles generated in water pool boiling. Condensing bubble behavior is affected by many parameters such as: working fluid, miscibility, bubble shape, bubble size, fraction of non-condensable gases, surface mobility, heat transfer, inertia and etc. For short duration of experiment and complexity of phenomenon, it is impossible to obtain detailed information about bubble mechanism through experimental data because the shape and the area of bubble interface are in exposure of rapid changes. Therefore, numerical simulation of vapor bubble is vital as complement to experiments. Tian et al. [45] simulated single steam bubble condensation behaviors in subcooled water using the Moving Particle Semi-implicit (MPS) method in axisymmetric domain. Pan et al. [35] applied the Volume of Fluid for simulation of single condensing bubble in subcooled boiling flow within two different vertical rectangular channels. Zeng et al. [51] employed a couple of level set method and volume of fluid (CLSVOF) in three-dimensional domain to study the effect of initial bubble sizes and subcooled temperatures on bubble condensation. Bahreini et al. [8] studied the effect of velocity and temperature gradient in vapor bubble rising during condensation using VOF method.

As there is no study of bubble rising in saturated pool boiling in the literature, in present study, the superheat vapor bubble rising in saturated quiescent water is simulated. The numerical model is implemented in OpenFOAM [50]. This numerical model is previously applied for simulation of saturation vapor bubble rising in subcooled liquid [40].

2 Mathematical model

2.1 Governing equation

For simulation of two phase flow with the phase change, the governing equations in one-fluid method are:

1. The global continuity equation

$$\frac{\partial}{\partial t}(\rho) + \nabla \cdot (\rho \overrightarrow{U}) = 0 \tag{4}$$

In boiling or condensation, mass transfer from one phase to the other is a local phenomena and it does not changes the global continuity equation.

2. The momentum equation

$$\frac{\partial(\rho \overrightarrow{U})}{\partial t} + \nabla \cdot (\rho \overrightarrow{U}\,\overrightarrow{U}) - \nabla \cdot (\mu(\nabla \overrightarrow{U}^T + \nabla \overrightarrow{U})) = -\nabla P + \rho \overrightarrow{g} + \sigma \kappa \nabla \alpha_L \tag{5}$$

Last term in right hand of Eq. 5 indicates surface tension force between two phases. σ is surface tension and κ is interface curvature. The surface tension is accounted by continuum surface force model (CSF) without the density averaging proposed by [13]. Curvature is defined as:

$$\kappa = -\nabla \cdot \left(\frac{\nabla \widetilde{\alpha_L}}{|\nabla \widetilde{\alpha_L}|} \right) \tag{6}$$

where $\widetilde{\alpha_L}$ is calculated from the VOF function α by smoothing it twice over a finite region around the interface using Lafaurie filter [26]. The usage of $\widetilde{\alpha_L}$ instead of α is reducing parasite currents up to one order [20].

As both phases are assumed incompressible, the equation for pressure is derived from continuity and momentum equations and given by:

$$\nabla \cdot \left(\frac{1}{A_D} \nabla p \right) = \nabla \cdot \phi - \dot{m}''' \left(\frac{1}{\rho_G} - \frac{1}{\rho_L} \right) \tag{7}$$

where A_D is diagonal entries of the momentum matrix equation following the approach of [50] and ϕ is the cell-face volume fluxes.

3. Energy equation

$$\frac{\partial}{\partial t}(T) + \nabla.(UT) - \nabla.(D_k \nabla T) = -D_c \dot{m}''' \times (H_{LG} + (C_L - C_G) T_{sat}) \tag{8}$$

The last terms in the right hand of Eq. 7 is added to energy equation during phase change. Usually the value $(C_{pL} - C_{pG})T_{sat}$ is negligible versus of latent heat. In order to keep the numerical stability D_k and D_c are defined as:

$$D_c = \frac{1}{\rho_L C_L \alpha_L + \rho_G C_G (1 - \alpha_L)} \tag{9}$$

4. Interface advection:

$$D_k = \frac{k_L \alpha_L + k_G (1 - \alpha_L)}{\rho_L C_L \alpha_L + \rho_G C_G (1 - \alpha_L)} \tag{10}$$

The transport equation for interface is derived from continuity equation and it is defined as [40]:

$$\frac{\partial \alpha_L}{\partial t} + \overrightarrow{U} \cdot \nabla \alpha_L + \nabla \cdot (\alpha_L(1-\alpha_L)\overrightarrow{U_c}) = -\dot{m}'''\left[\frac{1}{\rho_L} - \alpha_L\left(\frac{1}{\rho_L} - \frac{1}{\rho_G}\right)\right] \tag{11}$$

where α_L is the VOF function and is defined as:

$$\alpha_L(\overrightarrow{x}, t) = \frac{V_{Liquid}}{V} = \begin{cases} 1\,\overrightarrow{x} \in \text{liquid region} \\ 0 < \alpha_L < 1\ \overrightarrow{x} \in \text{interface region} \\ 0\,\overrightarrow{x} \in \text{gas region} \end{cases} \tag{12}$$

As there is no interface reconstruction in present study, interface is a region between two to three cells, Therefore, iso-contour $\alpha_L = 0.5$ represents interface position. The thermo physical properties of two immiscible fluids such as viscosity (μ), density (ρ) and thermal conductivity (k) are calculated using a weighted average:

$$y = \alpha_L y_L + (1.0 - \alpha_L) y_G, \quad y \in [\rho, \mu, k] \tag{13}$$

$\overrightarrow{U_c}$ in Eq. 11 is compressive velocity. It is computed in the normal direction to the interface to avoid any dispersion.

$$\overrightarrow{U_c} = \min\{C_\alpha |U|, \max(|U|)\}\frac{\nabla \alpha_L}{|\nabla \alpha_L|} \tag{14}$$

Additionally, a compressive factor (C_α) is applied to increase compression. This factor controls the weight of the compression flux. It is usually in the range of unity ($1.0 < C_\alpha < 4.0$) [10, 41]. In present study the compression factor $C_\alpha = 1.0$ is considered.

In order to close governing equations, an accurate phase change model is necessary. In present study phase change model proposed by Tanasawa [44] is employed. The volumetric transferred mass (kg/m^3 s) at the liquid–vapor interface is given by:

$$\dot{m}''' = \frac{2\gamma}{2-\gamma}\sqrt{\frac{1.0}{2\pi R}}\frac{\rho_G H_{LG}(T - T_{sat})}{T_{sat}^{3/2}}\nabla \alpha_L \tag{15}$$

where $T_{Sat}(P)$ is local saturation temperature, and γ is the fraction of molecules transferred from one phase to the other during phase change. $\gamma = 1.0$ is assumed in present study. $\gamma = [0.1 - 1]$ is recommended for dynamically renewing water surfaces such as jets or moving films [30].

The slight variation of saturation temperature as a function of local pressure P is considered by simplified Clausius–Clapeyron equation.

$$\ln\frac{P_{sat,1}}{P_{sat,0}} = -\frac{MH_{LG}}{R}\left(\frac{1}{T_{sat,1}} - \frac{1}{T_{sat,0}}\right) \tag{16}$$

2.2 Numerical details

The overall solver algorithm which is implemented on OpenFOAM220 is displayed in Fig. 2. Time step is calculated adaptively to assure CFL condition and the smallest temporal scale in computational domain which defined by user [10]. The volume fraction advection equation is solved using the multidimensional universal limiter with explicit solution (MULES) method [49]. Then program solve momentum equation to guess velocity field, then it enters the pressure–velocity loop known PISO [23] to calculate pressure and correct velocity. The loop repeated for multiple iterations (three times here) at each time step. In order to avoid a checker-boarding effect in the momentum equation, the Rhie-Chow momentum interpolation [38] is applied. Finally energy equation is solved. The applied discretisation schemes and the parameters of the numerical model are summarized in Table 2. For convenience, the corresponding terminology of OpenFOAM is given.

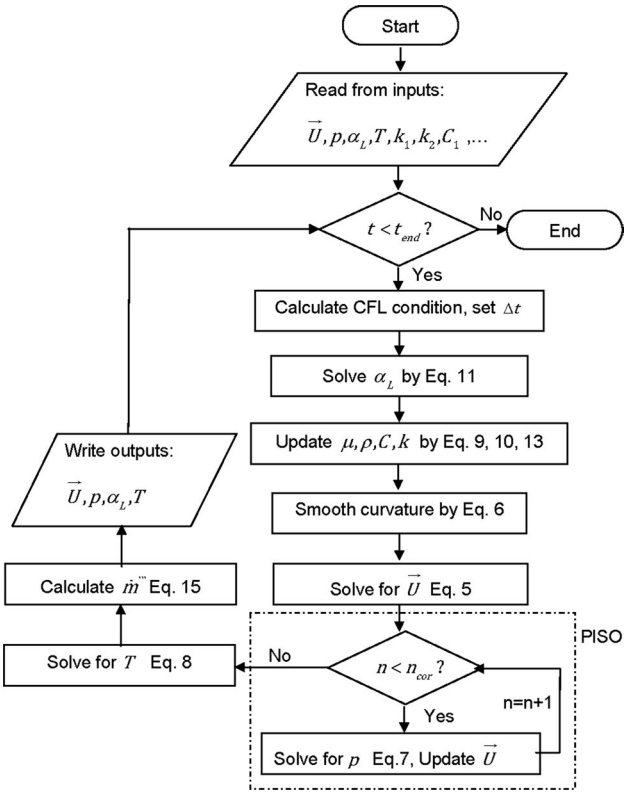

Fig. 2 Numerical model algorithm

2.3 Validation problems

In order to verify the present numerical model, two problems are presented. The isothermal bubble rising simulation shows the capability of present VOF method to correct predict the shape and terminal velocity of bubble rising. The second problem is the condensation of vapor near horizontal plate and forming the liquid film on. It shows the accuracy of phase change model.

Table 2 Discretisation schemes

Term	Discretisation scheme	Method
$\frac{\partial}{\partial t}(\rho\vec{U}),\ \frac{\partial}{\partial t}(\rho\vec{U}T)$	Euler	The first order bounded implicit scheme
$\nabla\cdot(\rho\vec{U}\vec{U})$	vanLeerV	Similar to VanLeer scheme [47] modified for vector field
$\nabla\cdot(\vec{U}\alpha_L),\nabla\cdot(\rho\vec{U}T)$	vanLeer	See [47]
$\nabla.\cdot\vec{U_c}\alpha_L(1-\alpha_L))$	InterfaceCompression	See [49]
$\nabla\chi^*$	Linear	Central difference schemes
$\nabla\frac{1}{f}^{**}\chi$	Corrected	Surface normal gradient with correction on non-orthogonal meshes [24]
$\nabla\cdot(\chi_1\nabla\chi_2)$	Linear corrected	Face values (χ_1) approximated by central difference scheme, and the resulting surface normal gradient is calculated using central difference schemes with non-orthogonal correction

Term	Interpolation scheme	Method
χ_f	Linear	Default interpolation schemes for getting face values from cell values

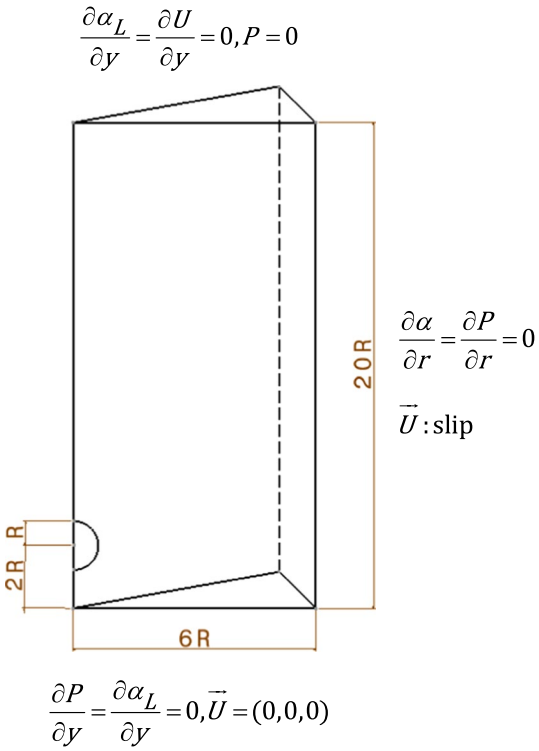

Fig. 3 Schematics and boundary condition of iso-thermal bubble rising

2.3.1 *Isothermal bubble rising*

In this section bubble rising in quiescent liquid is simulated. Four bubble regimes (C, G, E and H) are chosen based on Behaga charts [11] in Fig. 1. Depending on the Bond and Morton numbers different bubble trajectories including rectilinear, zigzag, spiral and helical paths may be observed. In present study bubble trajectory is rectilinear, therefore a 2-dimensional axisymmetric domain is considered for simulation to reduce computational cost. The schematic of problem and boundary conditions are illustrated at Fig. 3. At the lower side a no slip boundary condition, at side patch slip boundary condition and at upper side outflow boundary condition are applied. The computational width has a confinement effect on terminal velocity of single bubble rising [32]. To avoid the effect the computational domain width on numerical result, the computational domain with $W\times H=3D\times 10D$ are chosen. The chosen criteria is broadly in line with other free rise studies [1, 6, 14, 34]. The thermophysical properties are displayed in Morton and Bond number at Table 3. Viscosity ratio and density ration is 1000 and 10, respectively similar to Bower's numerical study [5]. The surface tension is

Table 3 Fluid physical properties and bubble characteristics

Case	D_0 (mm)	ν_L (μm^2/s)	*Mo*	*Bo*	Re_{Bhaga}	Re_{Bower}	$\mathrm{Re}_{present}$
C	4.506	11.98	8.2E−04	32	55.3	51.7	46.05
D	12.34	282.7	260	240	7.8	6.2	7.07
G	14.69	180	43	340	18.3	15.2	15.82
H	20.150	180	43	640	30.3	26.8	23.92

6.22E−03 N/m and the gravity acceleration is 9.81 m/s^2 in following simulations.

In order to analysis of mesh, three grids with 75 × 250, 150 × 500 and 300 × 1000 cells are considered. The discretization error between successively refined grids is calculated with reference to the finer mesh. For a quantity ψ the grid discretization error is defined as:

$$E_\phi = 100 \times \frac{|\psi_{\Delta x} - \psi_{\frac{\Delta x}{2}}|}{\psi_{\frac{\Delta x}{2}}} \tag{17}$$

The subscript $\frac{\Delta x}{2}$ represents finer mesh. In present study, ψ is considered terminal velocity. The bubble velocity is given by:

$$U_b = \frac{r_c^{n+1} - r_c^n}{\Delta t}, \quad r_c = \frac{\int r(1.0 - \alpha_L) dV}{\int (1.0 - \alpha_L) dV} \tag{18}$$

where r_c is the position of bubble center. The descrtization error and terminal velocity on different grids for case D and H are displayed at Table 4. In both cases, reductions in the discretization of 1% or less are achieved by refining mesh from grid 150 × 500 to grid 300 × 1000. Therefore, the grid with 150 × 500 cells corresponding to 50 cells per bubble diameter is used thereafter.

The shape of bubble is compared against experimental data [11] and previous three-dimensional numerical simulation [5] in Fig. 4. Reynolds numbers are compared in Table 3. There is reasonable agreement between current computation and experimental data and Bower's numerical study. There is a difference in viscosity ratio between current numerical simulation and experimental data which causes underestimation of Re number in our simulations. Higher viscosity ratio results in higher terminal velocity [5].

The coefficient of drag for a bubble rising in an initially stagnant liquid is derived from a force balance in vertical condition (Eq. 19). A spherical-equivalent bubble diameter is used. As a consequence, the effect of the bubble shape is implicitly lumped in the drag force coefficient, yielding a practical closure (Eq. 20):

$$\sum F_{total} = F_b + F_d = (\rho_L - \rho_G) g V_b + \frac{1}{2} \rho_L U_{rel}^2 A_b C_d = m_b a_b \tag{19}$$

$$C_d = \frac{(\rho_L - \rho_G) g - \rho_G a}{0.5 \rho_L U_{rel}^2} \left(\frac{V_b}{A_b} \right) \tag{20}$$

where V_b is bubble volume,A_b is projected area normal bubble direction, and $\left(\frac{V_b}{A_b}\right)$ is $\frac{2}{3} D_0$ for spherical-equivalent bubble. U_{rel} is bubble relative velocity. Liquid is stagnant, so U_{rel} is bubble velocity and computed from Eq. 18. The density ratio is 1000 in current simulations, hence the value of $\frac{\rho_G a}{0.5 \rho_L U_{rel}^2} \left(\frac{V_b}{A_b}\right)$ is negligible.

Table 4 Mesh convergence analysis of bubble in free rise

Case	Terminal velocity (cell numbers)			Discretization errors	
	75 × 250	150 × 500	300 × 1000	E_1	E_2
D	0.1507	0.1609	0.1621	6.28	0.0182
H	0.2131	0.2178	0.2238	2.809	0.167

The bubble drag coefficient (C_d) is obtained from Eq. 20 is plotted against time in Fig. 5. U_{rel} is infinitesimal at first, so the coefficient of drag is infinite. As bubble velocity increases, drag coefficient reduces to reach a steady value. Based on current simulations, the final drag coefficient of bubble is plotted against bubble Reynolds number on a log–log scale coordinate as shown in Fig. 6. The standard drag coefficient for rigid spheres is calculated from Eq. 21 [9] and is represented by a dash line in Fig. 6. Bhaga proposed a correlation (Eq. 22) between C_d and Re based on experimental, it is represented by a solid line in Fig. 6. The comparison shows a good agreement between current simulation and Bhaga correlation [11].

$$Cd = \begin{cases} \frac{24}{Re} & Re \le 1 \\ \frac{24}{Re}[1 + 0.102 Re^{0.955}] & 1 < Re \le 2 \\ \frac{24}{Re}[1 + 0.115 Re^{0.802}] & 2 < Re \le 21 \\ \frac{24}{Re}[1 + 0.189 Re^{0.632}] & 21 < Re \le 200 \\ 0.28 + \frac{6}{Re}^{0.5} + \frac{21}{Re} & 200 < Re \le 4000 \end{cases} \tag{21}$$

$$Cd = \left(2.67^{0.9} + \left(\frac{16}{Re} \right)^{0.9} \right)^{\frac{1}{0.9}}, \quad Mo > 4 \times 10^{-3} \tag{22}$$

2.3.2 *Film condensation on horizontal plate*

In this section, saturated vapor nearby a subcooled isothermal plate at T_w condenses to form a liquid film. If a linear temperature profile from T_w at the lower wall to T_{sat} at the interface is assumed, a control volume analysis leads to an analytical solution for the film thickness $\delta(t)$: [37]

$$\delta_{an}(t) = \left[2t \frac{k_L}{\rho_L C_L} \left(\frac{1}{2} + \frac{H_{LG}}{C_L \Delta T} \right)^{-1} \right]^{1/2} \tag{23}$$

Relevant thermo physical properties is for saturated water at $P_{sat} = 1$ Mpa. The computational domain represents a section of an infinitely wide condensing film, a quasi 1D computational domain with only one grid cell in the direction of translational invariance is considered. The top free stream boundary is set to saturation temperature ($T_{sat} = 453.03$ K) and the bottom wall is 30 K subcooled.

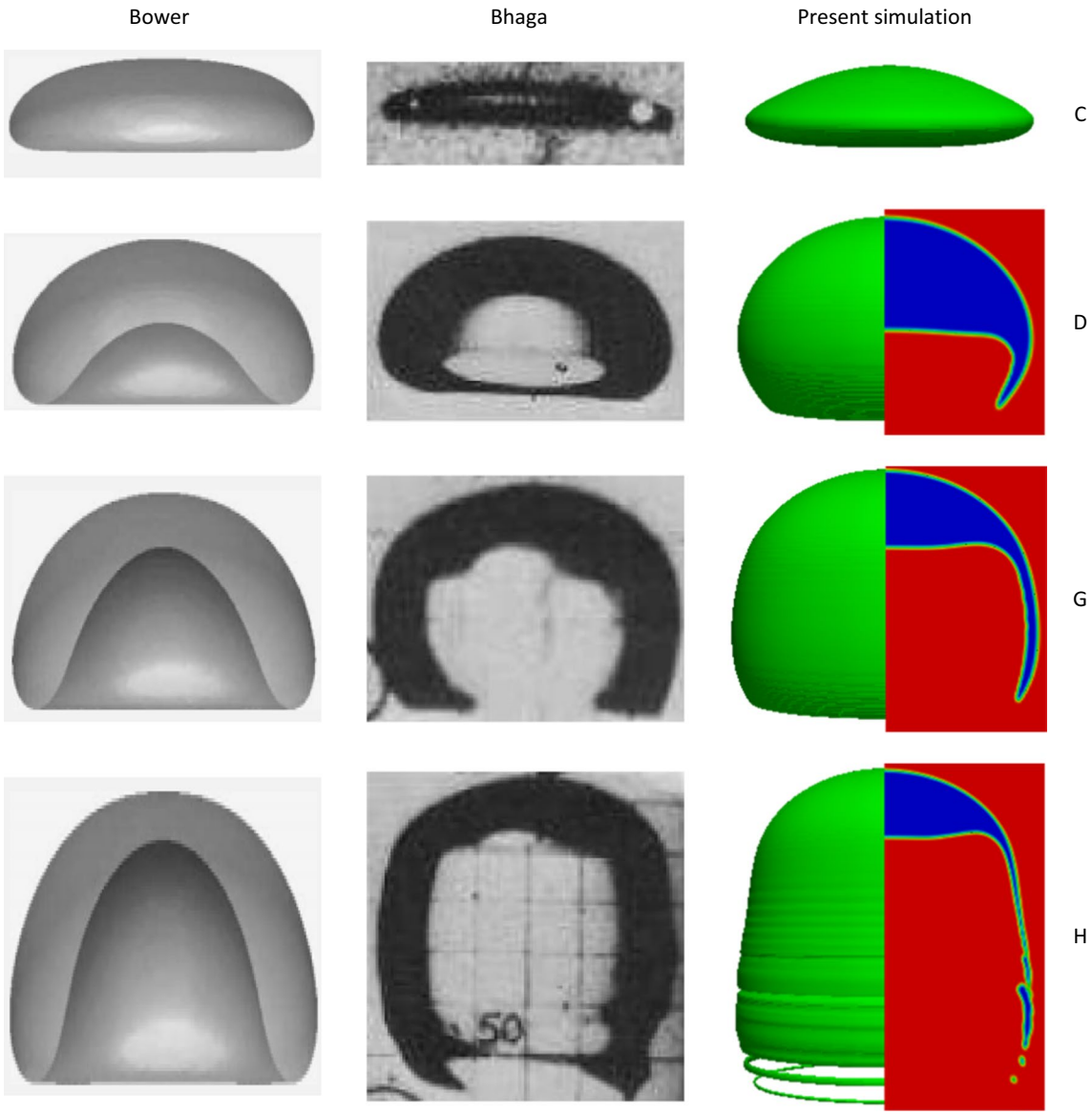

Fig. 4 Bubble shape for cases (C, D, G and H) from present simulation versus Bhaga experimental data [11] and Bower 3D-simulation [5]

All fluid entering through the free-stream boundary is vapor. In the beginning of simulation a very thin film is inserted in computational domain (Fig. 7).

The development of the liquid film thicknesses is illustrated in Fig. 8. The error is defined as the difference between film thickness from current numerical data and analytical solution. The integrated error is defined as:

$$E = \sum_{i} |\delta_{sim} - \delta_{an}| \Delta t \tag{24}$$

The thickness of condensate film is presented at Table 5 on different grids. It indicates an excellent agreement between the present numerical model and analytical solution.

3 Results and discussion

When a liquid is in contact with a surface maintained at a temperature above the saturation temperature of the liquid, boiling will eventually occur at that liquid–solid interface. Vapor density is smaller than liquid, so Rayleigh–Taylor instability occurs which amplifies small perturbations at interface and leads to bubble growth and detachment. In saturated pool boiling, liquid bulk temperature is in saturation temperature and the vapor bubble is superheat. In order to better understand the mechanism of saturated pool boiling, the rising of a single superheated vapor bubble in quiescent saturated water is simulated in this section.

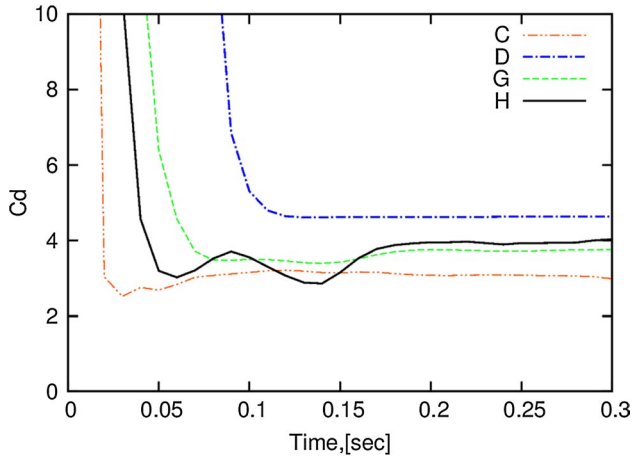

Fig. 5 The drag coefficient of iso-thermal bubble obtained from Eq. 20

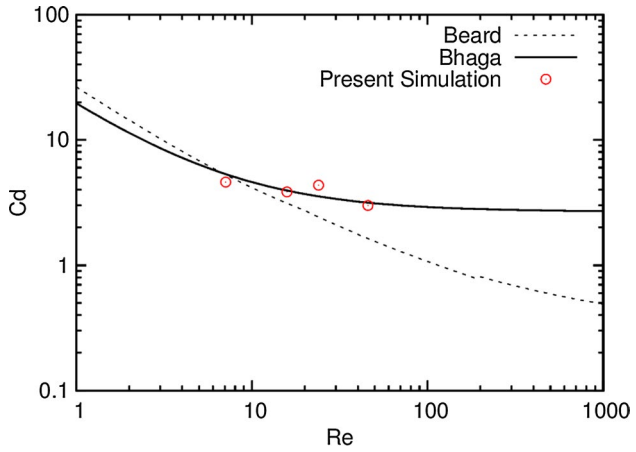

Fig. 6 Comparison of drag coefficient versus Re

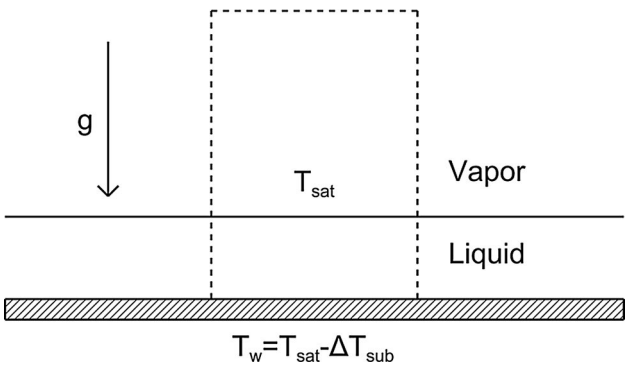

Fig. 7 Horizontal film condensation, $P_{sat} = 1$ Mpa, $\Delta T_{sub} = 30$ K

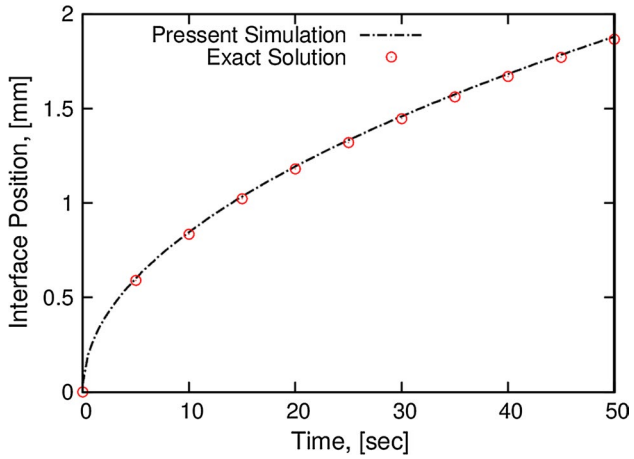

Fig. 8 Film thickness in horizontal film condensation, compare Exact solution with present numerical simulations $P_{sat} = 1$ Mpa and $\gamma = 1.0$

Table 5 Convergence study on horizontal film condensation

	Numerical simulation (cell numbers)			Exact
	128	256	512	
Film thickness (mm)	0.469314	0.471797	0.47051	0.467829
Error (μm s)	28.1	24.4	21.6	

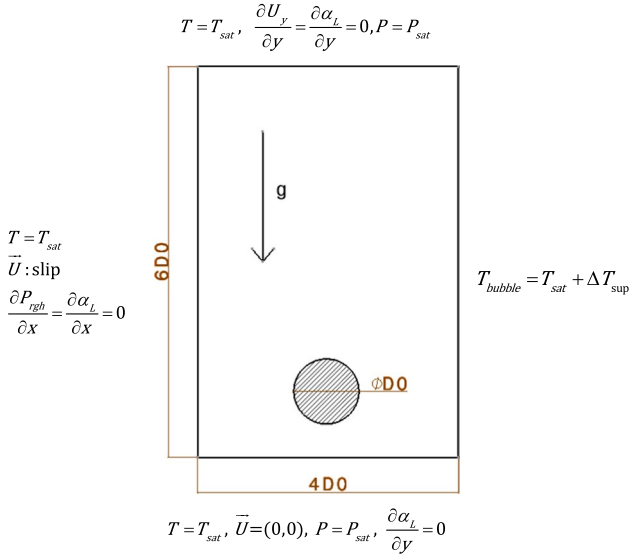

Fig. 9 Schematic of bubble condensation in subcooled boiling, initial and boundary conditions

3.1 Problem description

The geometry of the considered problem is illustrated in Fig. 9. The 2-dimensional space domain is set as $4D_0 \times 6D_0$ where D_0 is the initial diameter of vapor bubble. The bubble is located in the position of $(2D_0, D_0)$ at the beginning of simulation. Relevant thermo physical properties is for saturated water at $P_{sat} = 0.13$ Mpa corresponding high density ratio of $\frac{\rho_L}{\rho_v} \approx 1260$. It should be noted that the solver is capable of 3D simulation. In order

to simulate 2D simulation using OpenFOAM, special boundary condition called empty is applied in front and back faces.

3.2 Mechanism of vapor bubble rising in saturated liquid

In order to understand the mechanism of superheated vapor bubble rising in saturated liquid. Vapor bubble with initial diameter of 1 and 4 mm is simulated in different superheat temperatures. The bubble size history is illustrated in Fig. 10 for superheat temperatures ($\Delta T_{\text{sup}} = 10, 20, 40, 80\,\text{K}$). The vapor bubble equivalent diameter is normalized with bubble initial diameter (D_0). It is defined as:

$$D_{eq} = \sqrt{4\frac{\int (1-\alpha_L)dA}{\pi}} \tag{25}$$

The vapor bubble size increases initially then it begins losing the volume and it eventually collapses. The bubble with higher initial superheat temperature becomes bigger in early stage. Increase in bubble size is much obvious in Fig. 10a. The bubble with greater size would have longer life time and it goes upward further as shown in Fig. 11a, b. The bubble rising velocity is reduced with increase in superheat temperature. As bubble size decreases due to condensation, bubble rise upward faster.

The pressure increases linearly in liquid column due to hydrostatic term as shown in Fig. 12. There is a pressure difference between bubble up and bottom face which creates a net force in upward direction. This net force called buoyancy force accompanied with surface tension determines the bubble shape. Additionally, it is seen the surface tension is making the pressure inside vapor bubble higher than surrounding liquid.

Velocity vector is upward inside vapor bubble in Fig. 13. When the vapor bubble moves up, the empty space in the backward of bubble is filling with water. Hence, the vortex is created around bubble which becomes stronger in time

The bubble shape sequence is displayed at Fig. 14. In contrast with isothermal air bubble rising which reaches steady state shape, vapor bubble morphology changes and different bubble shapes are observed such as disk-like, ellipsoidal, wobbling and eventually spherical shape.

The dimensionless temperature ($\theta = \frac{T_b - T_L}{T_{bi} - T_L}$) is illustrated at Fig. 15. The vapor bubble undergoes different phase change phenomena. At first, the whole vapor bubble is at superheat temperature as shown in Fig. 16. There is a high gradient of temperature across the interface initially which results in a great heat flux from the superheated vapor bubble to saturated liquid. The vapor bubble temperature is higher than local saturation temperature, so liquid around bubble evaporates and bubble size increases.

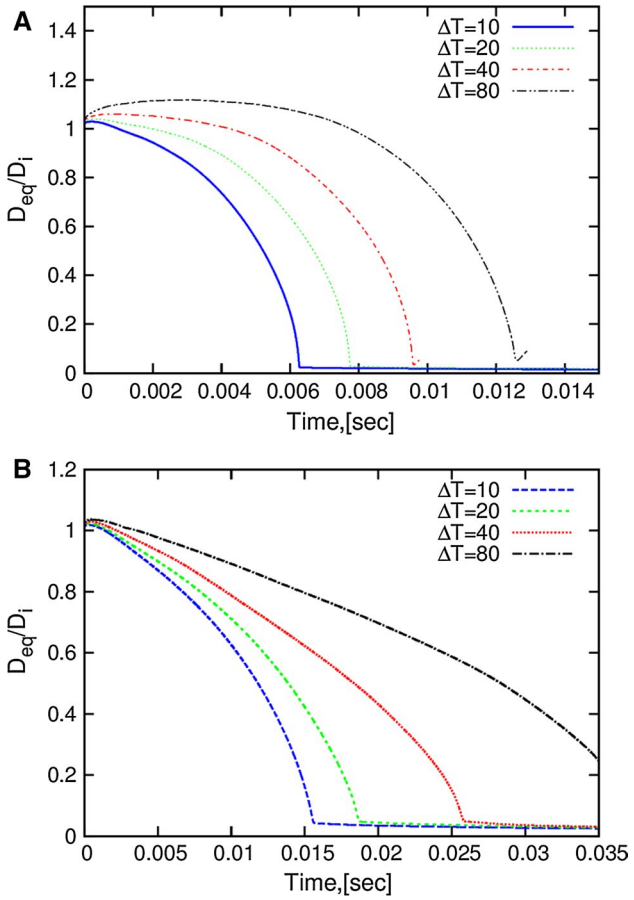

Fig. 10 Bubble size history for $D_0 = 1\,\text{mm}, 4\,\text{mm}$, $P_{sat} = 0.13\,\text{Mpa}$

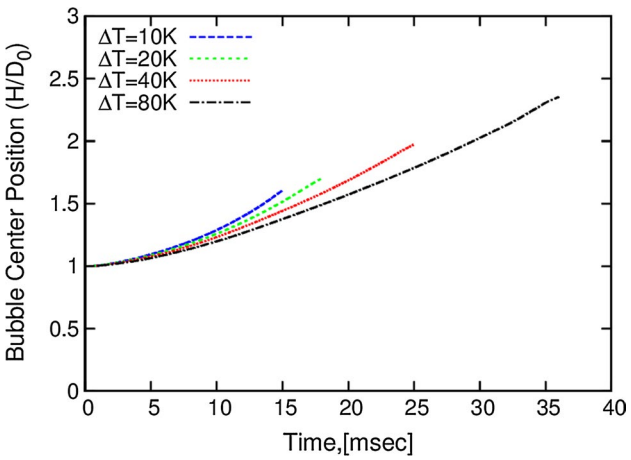

Fig. 11 Bubble center position for $D_0 = 4\,\text{mm}$, $P_{sat} = 0.13\,\text{Mpa}$

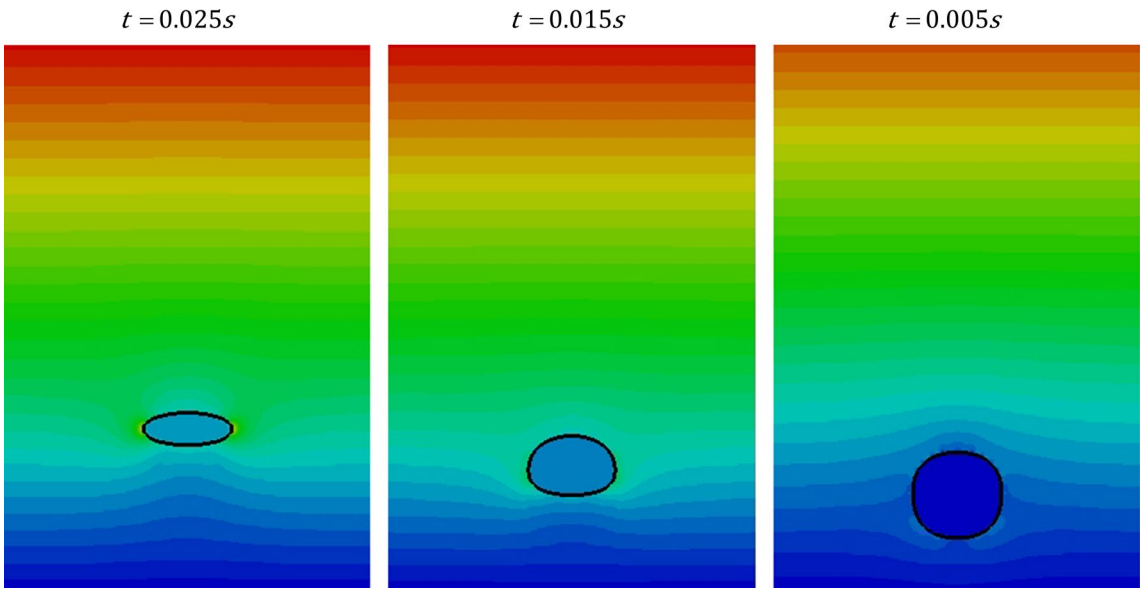

Fig. 12 Pressure contour in vapor bubble rising $D_0 = 4\,\text{mm}$, $P_{sat} = 0.13\,\text{Mpa}$

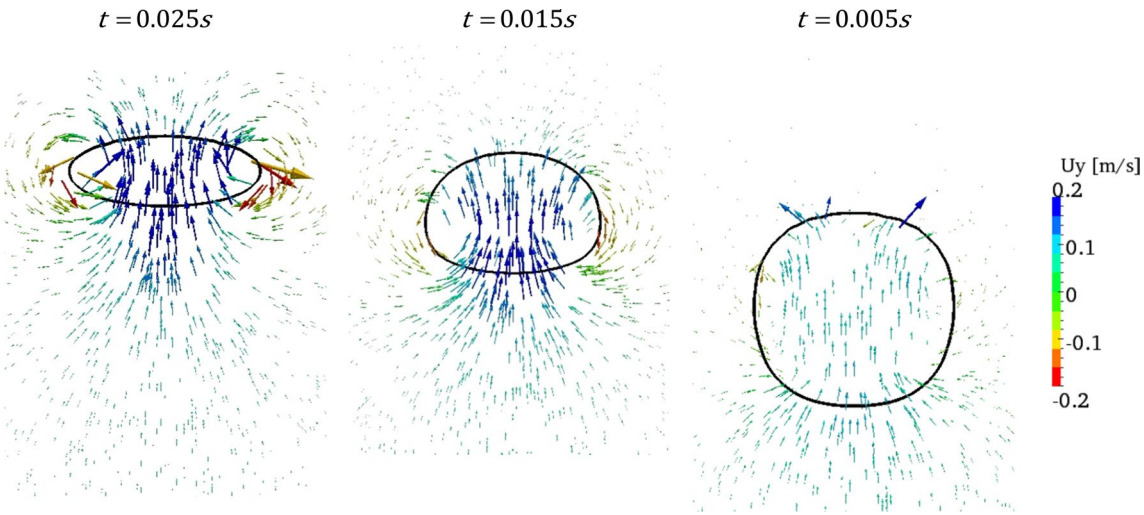

Fig. 13 Velocity field in vapor bubble rising $D_0 = 4\,\text{mm}$, $P_{sat} = 0.13\,\text{Mpa}$

Boiling is endothermic process. Therefore, bubble temperature drops rapidly. When the temperature inside vapor bubble reaches the saturation temperature of liquid around bubble at the region nearby the interface, the condensation process begins. The saturation temperature is a function of thermodynamic pressure. The pressure inside vapor bubble is greater than surrounding liquid due to surface tension. Therefore, local saturation temperature is higher in vapor bubble. The vapor at interface based on local saturation temperature is subcooled and begins condensing. As condensation is exothermic process, it is seen vapor bubble temperature drops at lower rate than previous stage. The bubble condensation is accelerated in the final stage, because the ratio of area to volume increases. Additionally, pressure inside bubble becomes higher leads into higher local saturation. These parameters increase phase change rate.

The Figs. 17 and 18 display bubble life time as a function of vapor bubble initial diameter (D_0) and superheat temperature (ΔT_{sup}), respectively. It is observed that bubble life time has a quasi linear relation with bubble size, because the key parameter in heat transfer from superheated vapor bubble to saturated liquid is the ratio of vapor volume to area which has a linear relation with diameter. Also bubble life time increases almost linearly with increment in superheat temperature; because the

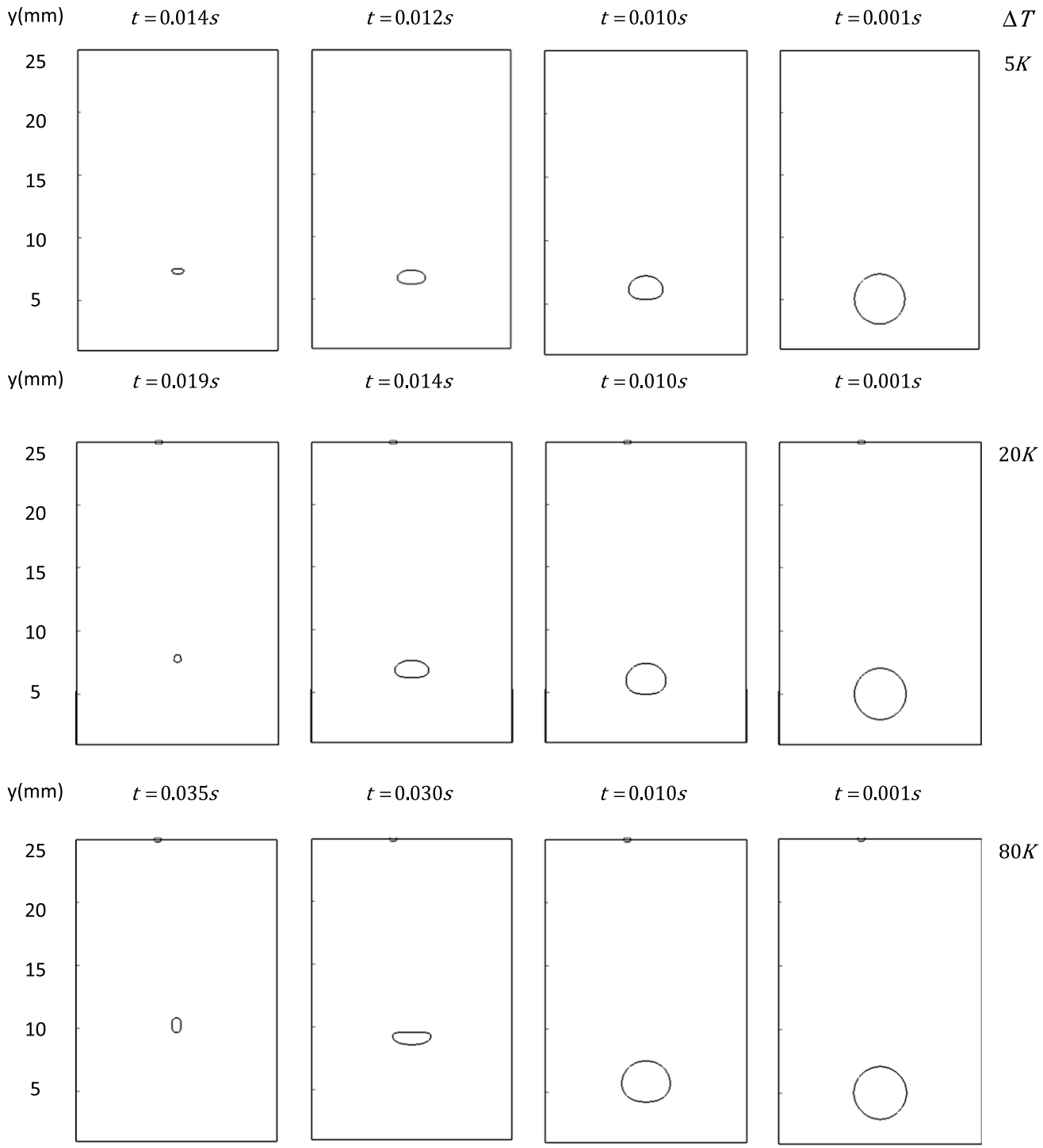

Fig. 14 Bubble shape sequence for $D_0 = 4$ mm, $P_{sat} = 0.13$ Mpa

amount of transferred mass based on Tanasawa model (Eq. 15) is linear proportional to temperature difference. It should be noted that further study should be made for other cases with different operating conditions to reach a general correlation for bubble life time based on superheat temperature and initial diameter.

3.2.1 Constant versus variable thermo-physical properties for vapor

In this section two sets of simulations are conducted to measure the validity of constant thermo-physical properties in pervious sections. The initial bubble diameter is

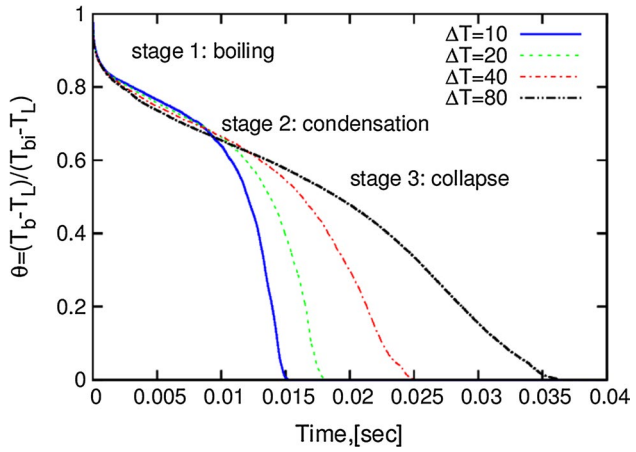

Fig. 15 Bubble dimensionless temperature for $D_0 = 4$ mm, $P_{sat} = 0.13$ Mpa

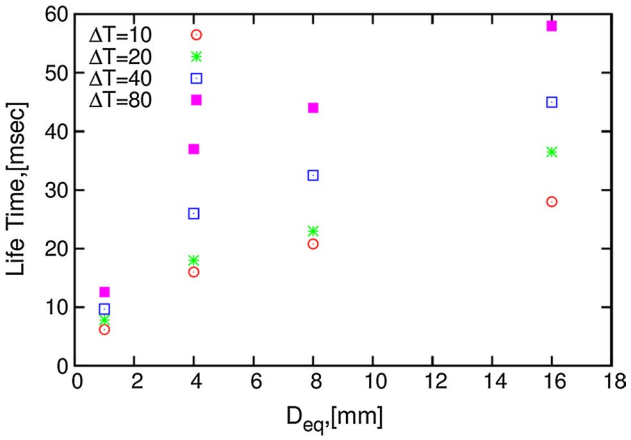

Fig. 17 Bubble life time for $P_{sat} = 0.13$ Mpa

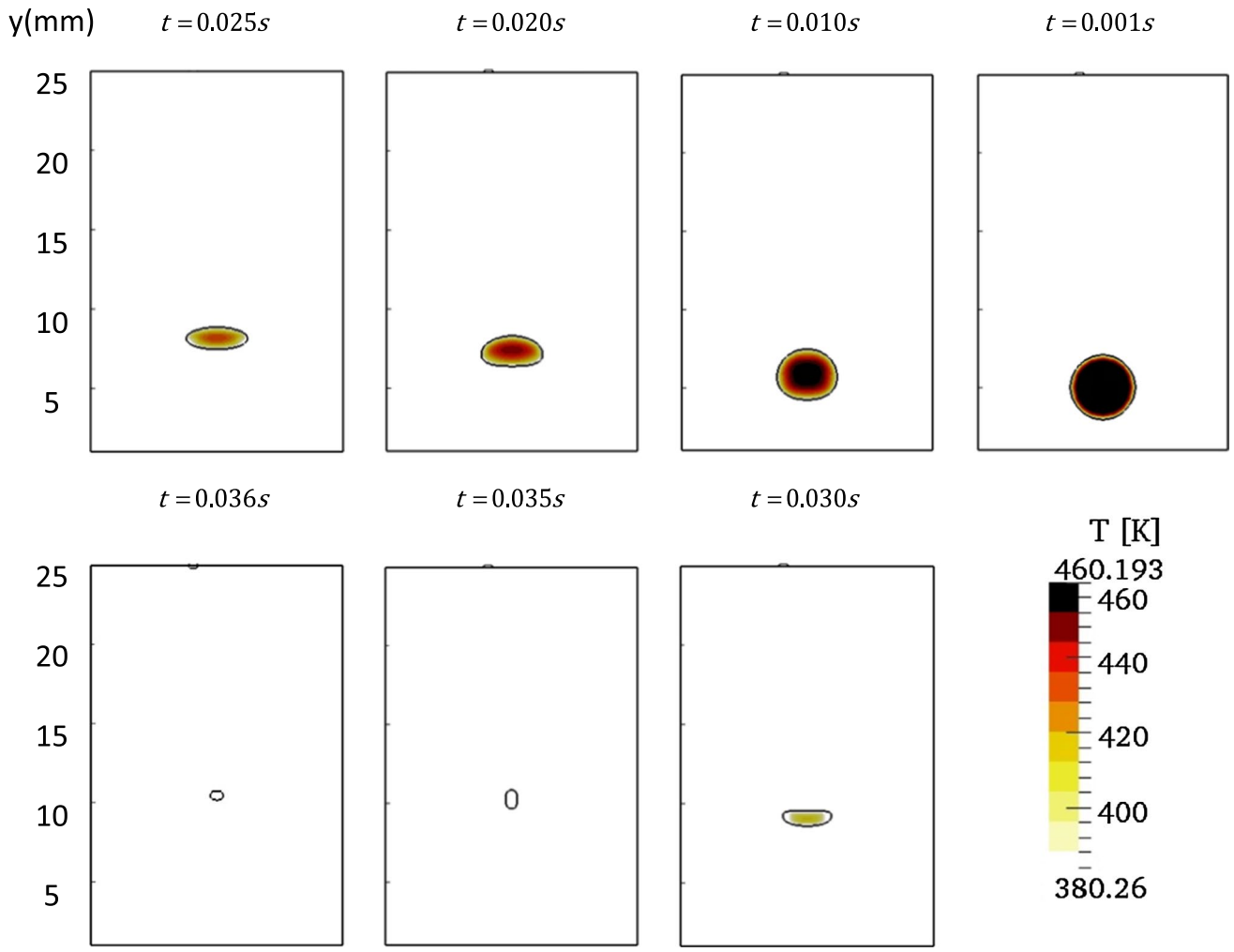

Fig. 16 Temperature contour for $D_0 = 4$ mm, $P_{sat} = 0.13$ Mpa, $\Delta T_{sup} = 80$ K

1 mm and simulation is conducted for four temperature difference {10, 20, 40 and 80 K}. In first set of simulation gas is assumed perfect gas, so density is a function of pressure and temperature as follow:

$$\rho = \frac{P}{RT} \tag{26}$$

Then in second set of simulation, other thermo-physical properties of vapor such as thermal conductivity, specific heat and viscosity is considered as variable function of temperature. The polynomial function is fitted on vapor properties in temperature range $T \in [380.26, 460.26]$. The vapor data at 0.13 MPa is obtained from NIST Chemistry WebBook [28].

$$y_v(T) = a_0 + a_1 T + a_2 T^2 + a_3 T^3 \tag{27}$$

where coefficients are listed in Table 6.

Result for bubble history is displayed at Fig. 19 for the worst case scenario which is related to the highest temperature difference. As the equation state of vapor is assumed perfect gas, the bubble life time is slightly longer than constant thermo-physical properties. However, when all properties are considered variable with temperature, the difference is marginal. Therefore, it seems reasonable to select constant thermo physical properties for vapor in present study.

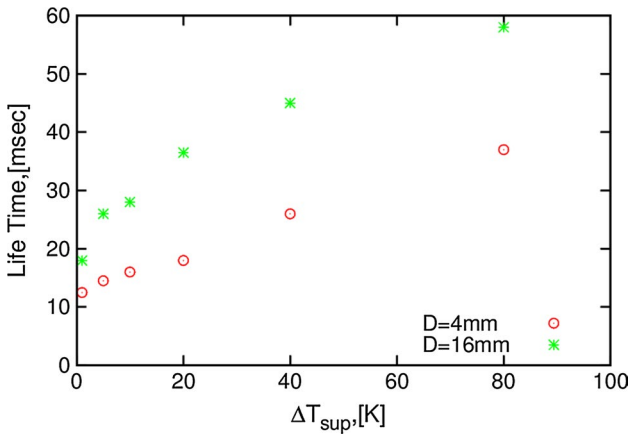

Fig. 18 Bubble life time versus superheat temperature

4 Concluding remarks

In present study, rising of superheat vapor bubble in saturated water is modeled using CF-VOF method in OpenFOAM. The numerical model is validated with analytical solution of film condensation on horizontal plate and with experimental data and correlations on isothermal bubble rising. These comparisons indicate the capability of present numerical model to accurate simulation of two-phase flow with phase change. The simulation of a single vapor bubble rising reveals some promising remarks:

1. Superheated vapor bubble in saturated liquid undergoes boiling and condensation.
2. Bubble life time has almost a linear relation with bubble size and bubble superheat temperature in present operating condition.
3. Increase in superheat temperature reduces vapor bubble rising velocity.

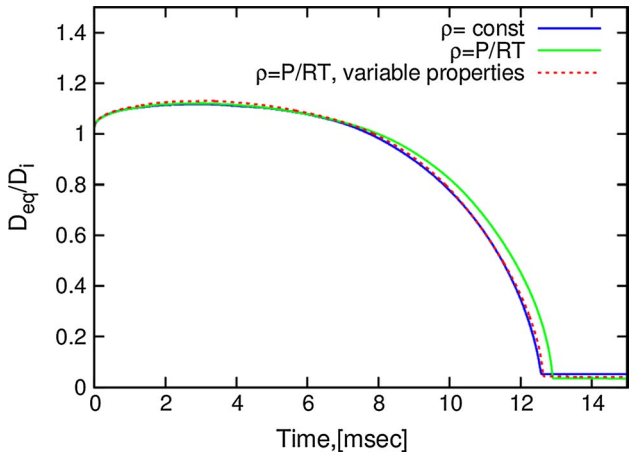

Fig. 19 Bubble life history for 3 vapor states: *1*-incompressibe ($\rho = const$), *2*-perfect gas ($\rho = \frac{P}{RT}$) and *3*-perfect gas ($\rho = \frac{P}{RT}$) with variable thermo-physical properties

Table 6 The coefficients of polynomial function for vapor properties

y_v	a_0	a_1	a_2	a_3
$k\left(\frac{\mathrm{w}}{\mathrm{mK}}\right)$	0.021645	−4.51572E−05	1.48117E−7	–
$C\left(\frac{\mathrm{kJ}}{\mathrm{kgK}}\right)$	24.8227	−0.151096	0.0003342	−2.47063E−07
μ (Pa s)	4.09844E−06	−8.4336E−10	7.97162E−11	−5.07776E−14

References

1. Albadawi A, Donoghue D, Robinson A, Murray D, Delauré Y (2014) On the assessment of a VOF based compressive interface capturing scheme for the analysis of bubble impact on and bounce from a flat horizontal surface. Int J Multiph Flow 65:82–97
2. Alhendal Y, Turan A (2015) Thermocapillary bubble dynamics in a 2D axis swirl domain. Heat Mass Transf 51:529–542
3. Alhendal Y, Turan A, Hollingsworth P (2013) Thermocapillary simulation of single bubble dynamics in zero gravity. Acta Astronaut 88:108–115
4. Alke A, Bothe D, Kröger M, Warnecke H (2009) VOF-based simulation of conjugate mass transfer from freely moving fluid particles. Comput Methods Multiph Flow V 63:157–168
5. Amaya-Bower L, Lee T (2010) Single bubble rising dynamics for moderate Reynolds number using lattice Boltzmann method. Comput Fluids 39:1191–1207
6. Ansari M, Nimvari M (2011) Bubble viscosity effect on internal circulation within the bubble rising due to buoyancy using the level set method. Ann Nucl Energy 38:2770–2778
7. Ansari MR, Azadi R, Salimi E (2016) Capturing of interface topological changes in two-phase gas–liquid flows using a coupled volume-of-fluid and level-set method (VOSET). Comput Fluids 125:82–100
8. Bahreini M, Ramiar A, Ranjbar AA (2015) Numerical simulation of bubble behavior in subcooled flow boiling under velocity and temperature gradient. Nucl Eng Des 293:238–248
9. Beard K, Pruppacher H (1969) A determination of the terminal velocity and drag of small water drops by means of a wind tunnel. J Atmos Sci 26:1066–1072
10. Berberović E, van Hinsberg NP, Jakirlić S, Roisman IV, Tropea C (2009) Drop impact onto a liquid layer of finite thickness: dynamics of the cavity evolution. Am Phys Soc 79:036306 (036315)
11. Bhaga D, Weber M (1981) Bubbles in viscous liquids: shapes, wakes and velocities. J Fluid Mech 105:61–85
12. Bothe D, Fleckenstein S (2013) A volume-of-fluid-based method for mass transfer processes at fluid particles. Chem Eng Sci 101:283–302
13. Brackbill JU, Kothe DB, Zemach C (1992) A continuum method for modeling surface tension. J Comput Phys 100:335–354
14. Chakraborty I, Biswas G, Ghoshdastidar P (2013) A coupled level-set and volume-of-fluid method for the buoyant rise of gas bubbles in liquids. Int J Heat Mass Transf 58:240–259
15. Chen Y, Mayinger F (1992) Measurement of heat transfer at the phase interface of condensing bubbles. Int J Multiph Flow 18:877–890
16. Clift R, Grace JR, Weber ME (1978) Bubbles, drops and particles. Academic Press, New York
17. Ellingsen K, Risso F (2001) On the rise of an ellipsoidal bubble in water: oscillatory paths and liquid-induced velocity. J Fluid Mech 440:235–268
18. Gumulya M, Joshi JB, Utikar RP, Evans GM, Pareek V (2016) Bubbles in viscous liquids: time dependent behaviour and wake characteristics. Chem Eng Sci 144:298–309
19. Harada T, Nagakura H, Okawa T (2010) Dependence of bubble behavior in subcooled boiling on surface wettability. Nucl Eng Des 240:3949–3955
20. Hoang DA, van Steijn V, Portela LM, Kreutzer MT, Kleijn CR (2013) Benchmark numerical simulations of segmented two-phase flows in microchannels using the volume of fluid method. Comput Fluids 86:28–36
21. Hua J, Lou J (2007) Numerical simulation of bubble rising in viscous liquid. J Comput Phys 222:769–795
22. Hua J, Stene JF, Lin P (2008) Numerical simulation of 3D bubbles rising in viscous liquids using a front tracking method. J Comput Phys 227:3358–3382
23. Issa RI (1986) Solution of the implicitly discretised fluid flow equations by operator-splitting. J Comput Phys 62:40–65
24. Jasak H (1996) Error analysis and estimation for the finite volume method with applications to fluid flows. Imperial College. University of London
25. Kulkarni AA, Joshi B (2005) Bubble formation and bubble rise velocity in gas–liquid systems: a review. Ind Eng Chem Res 44:5873–5931
26. Lafaurie B, Nardone C, Scardovelli R, Zaleski S, Zanetti G (1994) Modelling merging and fragmentation in multiphase flows with SURFER. J Comput Phys 113:134–147
27. Legendre D, Zenit R, Velez-Cordero JR (2012) On the deformation of gas bubbles in liquids. Phys Fluids (1994-present) 24:043303
28. Lemmon EW, McLinden MO, Friend DG (2016) Thermophysical properties of fluid systems. http://webbook.nist.gov
29. Maldonado M, Quinn J, Gomez C, Finch J (2013) An experimental study examining the relationship between bubble shape and rise velocity. Chem Eng Sci 98:7–11
30. Marek R, Straub J (2001) Analysis of the evaporation coefficient and the condensation coefficient of water. Int J Heat Mass Transf 44:39–53
31. Marschall H, Hinterberger K, Schuler C, Habla F, Hinrichsen O (2012) Numerical simulation of species transfer across fluid interfaces in free-surface flows using OpenFOAM. Chem Eng Sci 78:111–127
32. Mukundakrishnan K, Quan S, Eckmann DM, Ayyaswamy PS (2007) Numerical study of wall effects on buoyant gas-bubble rise in a liquid-filled finite cylinder. Phys Rev E 76:036308
33. Ohta M, Imura T, Yoshida Y, Sussman M (2005) A computational study of the effect of initial bubble conditions on the motion of a gas bubble rising in viscous liquids. Int J Multiph Flow 31:223–237
34. Ohta M, Sussman M (2012) The buoyancy-driven motion of a single skirted bubble or drop rising through a viscous liquid. Phys Fluids (1994-present) 24:112101
35. Pan L-M, Tan Z-W, Chen D-Q, Xue L-C (2012) Numerical investigation of vapor bubble condensation characteristics of subcooled flow boiling in vertical rectangular channel. Nucl Eng Des 248:126–136
36. Pivello MR, Villar M, Serfaty R, Roma A, Silveira-Neto A (2014) A fully adaptive front tracking method for the simulation of two phase flows. Int J Multiph Flow 58:72–82
37. Rattner AS, Garimella S (2014) Simple mechanistically consistent formulation for volume-of-fluid based computations of condensing flows. J Heat Transf 136:071501
38. Rhie C, Chow W (1983) Numerical study of the turbulent flow past an airfoil with trailing edge separation. AIAA J 21:1525–1532
39. Samkhaniani N, Ajami A, Kayhani MH, Dari AS (2012) Direct numerical simulation of single bubble rising in viscous stagnant liquid. In: International conference on mechanical, automobile and robotics engineering (ICMAR'2012)
40. Samkhaniani N, Ansari M (2016) Numerical simulation of bubble condensation using CF-VOF. Prog Nucl Energy 89:120–131
41. Samkhaniani N, Gharehbaghi A, Ahmadi Z (2013) Numerical simulation of reaction injection molding with polyurethane foam. J Cell Plast 49:405–421
42. Shew WL, Poncet S, Pinton J-F (2006) Force measurements on rising bubbles. J Fluid Mech 569:51–60
43. Sideman S, Hirsch G (1965) Direct contact heat transfer with change of phase: condensation of single vapor bubbles in

an immiscible liquid medium. Preliminary studies. AIChE J 11:1019–1025
44. Tanasawa I (1991) Advances in condensation heat transfer. Adv Heat Transf 21:55–139
45. Tian W, Ishiwatari Y, Ikejiri S, Yamakawa M, Oka Y (2010) Numerical computation of thermally controlled steam bubble condensation using moving particle semi-implicit (MPS) method. Ann Nucl Energy 37:5–15
46. Tripathi MK, Sahu KC, Govindarajan R (2015) Dynamics of an initially spherical bubble rising in quiescent liquid. Nat Commun 6:6268. doi:10.1038/ncomms7268
47. Van Leer B (1974) Towards the ultimate conservative difference scheme. II. Monotonicity and conservation combined in a second-order scheme. J Comput Phys 14:361–370
48. van Sint Annaland M, Deen N, Kuipers J (2005) Numerical simulation of gas bubbles behaviour using a three-dimensional volume of fluid method. Chem Eng Sci 60:2999–3011
49. Weller H (2008) A new approach to VOF-based interface capturing methods for incompressible and compressible flow. OpenCFD Ltd., Report TR/HGW/04
50. Weller HG, TaboraI G, Jasak H, Fureby C (1998) A tensorial approach to computational continuum mechanics using object-oriented techniques. Comput Phys 12:620–632
51. Zeng Q, Cai J, Yin H, Yang X, Watanabe T (2015) Numerical simulation of single bubble condensation in subcooled flow using OpenFOAM. Prog Nucl Energy 83:336–346